Determining tensile yield stresses from Small Punch tests: A numerical-based scheme

Peter Hähner [a,*], Celal Soyarslan [b], Betül Gülçimen Çakan [c], Swantje Bargmann [b]

[a] European Commission, Joint Research Centre, Directorate G: Nuclear Safety and Security, Westerduinweg 3, Petten 1755 LE, the Netherlands
[b] Chair of Solid Mechanics, University of Wuppertal, Gaussstr. 20, Wuppertal 42119, Germany
[c] Department of Mechanical Engineering, Uludağ University, Görükle, Bursa 16059, Turkey

HIGHLIGHTS

- A new self-consistent data reduction scheme is introduced for the determination of the tensile yield stress from Small Punch tests.
- The scheme derives from finite element simulations of a wide range of strength coefficients and hardening exponents of power-law hardening.
- The method is validated by comparing yield stress predictions to actual yield stresses, using various hardening laws and experimental data.
- With the new approach the uncertainty of yield stress determination by Small Punch tests can be largely reduced as compared to traditional schemes.

GRAPHICAL ABSTRACT
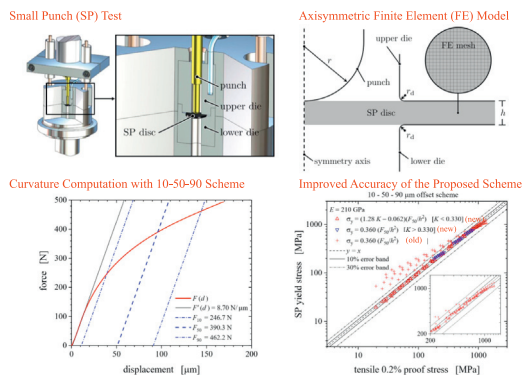
ARTICLE INFO

ABSTRACT

The Small Punch (SP) test serves the screening of mechanical material properties and their degradation in a virtually non-invasive way. It requires robust frameworks for the derivation of mechanical properties and microstructure–mechanical property correlation. The tensile yield stress σ_y is commonly associated with an elastic-plastic transition force F_e via $\sigma_y = \alpha F_e/h^2$ with h denoting the SP disc thickness and a dimensionless coefficient α considered constant. Here it is shown that α cannot be taken as a constant. Instead a new self-consistent data reduction scheme is proposed for the determination of σ_y which is based on the curvature of the force–displacement curve rather than a single F_e force level. The scheme derives from finite element simulations of a wide range of strength coefficients C and hardening exponents n of power law flow $\sigma = C\epsilon^n$. To a good approximation the scheme depends only on the hardening exponent n, which depends on the curvature, whereas C and the elastic modulus barely matter. The method is validated by comparing the yield stress predictions with the actually implemented yield stresses in the simulations, using various types of hardening rules, as well as experimental data. The uncertainty of yield stress determination by SP tests is thereby largely reduced as compared to the traditional scheme.

1. Introduction

Many components in power plants, e.g. pressure vessels and steam pipes, operate at demanding conditions causing gradual

* Corresponding author.
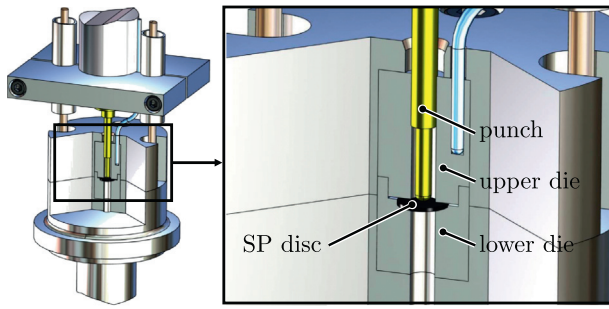*E-mail address:* peter.haehner@ec.europa.eu (P. Hähner).

Fig. 1. Schematic of the experimental set-up of a Small Punch test rig.

degradation of the material properties and mechanical performance required for structural integrity. Miniaturized test techniques like the Small Punch (SP) test enable assessing this degradation and, hence, the residual lifetime during which safe operation of a component can be ensured. Unlike conventional mechanical test methods SP testing requires sub-sized specimens only, thereby enabling the mechanical performance assessment of structural materials in a virtually non-invasive way.

SP tests also play an important role in that they allow for rapid screening of mechanical material properties, as well as the mechanical property determination of neutron irradiated materials while minimizing the amount of activated material to be tested. From a practical point of view, besides validated experimental methods, SP testing requires robust frameworks for the derivation of mechanical properties and microstructure–mechanical property correlations.

The typical SP test specimen is a disc with a thickness of 0.5 mm and a diameter of 8 mm being rigidly clamped, in order to be forced into a receiving circular hole of 4 mm diameter by means of a hemispherical punch (or ceramic ball) of 2.5 mm diameter, see Fig. 1. Different experimental set-ups are used for determining either tensile plastic and fracture mechanical properties (by tests performed at constant displacement rate), or creep properties (at constant force). In a Small Punch test of tensile properties, the punch tip or ball deforms the specimen at a constant displacement rate of the cross head, while the force F is recorded as a function of displacement and/or specimen deflection. If displacement is used, parasitic compliances of the test frame have to be taken into account and corrected for. The main output of the test is then a force–displacement curve.

Considerable effort has been made to translate the characteristics obtained from a force–displacement curve, in particular, elastic–plastic transition force and maximum force, into the conventional tensile yield stress and ultimate tensile strength [1-18]. This may involve empirical or semi-empirical correlations established between the mentioned quantities. However, the SP test still suffers from large uncertainties when it comes to deriving tensile properties from it, in particular, regarding the yield stress σ_y, which is commonly associated with an elastic–plastic transition force F_e via

$$\sigma_y = \alpha F_e / h^2 , \qquad (1)$$

with h denoting the initial SP disc thickness and a dimensionless coefficient α considered to be constant. For instance, this relation was used by Mao and Takahashi [6] who tested various austenitic and ferritic steels (see Table 1).

The elastic bending theory of plates can be used to analytically relate the tensile bending stress at the centre of the disc to the applied force. The yield stress can then be approximated from the deviation from linearity of the elastic part of the force–displacement

Table 1
Compilation of correlation factors $\alpha = h^2 \sigma_y / F_e$ proposed in the literature. Deviations from the conventional specimen size and die geometry are indicated in the last column.

Reference	Material, temperature	Method	$\alpha = h^2 \sigma_y / F_e$	Remark
Mao and Takahashi, 1987 [6]	Various austenitic and ferritic steels, RT	2-tangent	0.36	TEM specimen size ($d = 3$ mm, $h = 0.25$ mm $R = 0.75$ mm, $r = 0.5$ mm)
Kameda and Mao, 1992 [3]	Various austenitic and ferritic steels, $[-196°C, 200°C]$	2-tangent	0.36	$r = 1.2$ mm
Cheon and Kim, 1996 [9]	SA508 steel, 12 Cr Steel, RT	Offset $h/100$	0.59–0.62	$h = 0.5, 0.25$ mm ($R = 2$ mm, $r = 1.2$ mm)
Fleury and Ha, 1998 [5]	4 different austenitic and ferritic steels, $[25°C, 600°C]$	Not specified	0.33	$r = 1.2$ mm Square specimens 10×10 mm, $h = 0.5$ mm
Finarelli et al., 2004 [10]	316L stainless steel RT	2-tangent	0.38	TEM specimen size ($d = 3$ mm, $h = 0.25$ mm $R = 0.75$ mm, $r = 0.5$ mm)
Campitelli et al., 2004 [11]	316L and F82H, RT	2-tangent	0.39	TEM specimen size ($d = 3$ mm, $h = 0.25$ mm $R = 0.75$ mm, $r = 0.5$ mm)
Contreras et al., 2008 [12]	Ferritic-pearlitic AE460, $\{-60°C, -50°C\}$	Offset 50 μm $h/10$	0.43	TEM specimen size ($d = 3$ mm, $h = 0.25$ mm $R = 0.75$ mm, $r = 0.5$ mm)
Rodríguez et al., 2009 [13]	HAZ of weldment in 30CrMo5-2 plate, RT	Offset 50 μm $h/10$	0.38	CWA 15627-2007
Matocha et al., 2012 [7]	Carbon steel 22 K and heat treatments, RT	Offset 100 μm $h/5$	0.31	CWA 15627-2007
García et al., 2014 [2]	Wide variety of steels and one Al alloy, RT	Offset 50 μm $h/10$	0.346	CWA 15627-2007 Thickness corrected
Altstadt et al., 2016 [14]	T91 steels, RT and 300°C	2-secant	0.44–0.60	Result of a round robin
Janča et al., 2016 [16]	Various steels and Al alloys	$F_{e1.5}$	0.51	Eq. (3)
Davies et al., 2017 [18]	Laser deposited C263 Ni superalloy RT and 780°C	2-secant	0.37	CWA 15627-2007
Moreno 2018 [17]	Various Al alloys and structural steels, RT	($h/100, h/10$, 2-tangents, 2-secant),	0.23–0.98	Specimen thicknesses between 0.35 mm–0.6 mm

curve [4]. In the case of a constrained (i.e. rigidly clamped) disc specimen, and yielding occurring at the surface opposite to the punch, Vorlicek et al. [4] refer to a simplified relationship,

$$\sigma_y = 3\frac{F_e}{2\pi h^2} \,, \qquad (2)$$

in accordance with the generalized empirical Eq. (1) if $\alpha = 3/2\pi$. While several other linear relations have been proposed in the literature [19-21], the preferred form is Eq. (1) which shows that h^2 is a scaling parameter describing the thickness dependence. In the present paper, however, this approach is revisited and it is shown that α cannot be taken as a constant.

The elastic–plastic transition force F_e in those relations is regarded as the force level at which the deformation passes from elastic bending (noting that some amount of plastic indentation underneath the punch also occurs during this stage) to plastic bending. However, it is not obvious how this force level can reliably be derived from a force–displacement curve, and various methods are used to assign a value to F_e. The graphical methods to determine F_e are the offset method and the two-tangent method. The first method requires plotting a straight line at $h/10$ (i.e., using an offset of 50 μm for a conventional 0.5 mm disc) or $h/100$ offset [9,12,13,22] parallel to the initial linear part of the force–displacement curve $F(d)$ and taking F_e as the force value at the intersection of this parallel line and the force–displacement curve.

Generally, the initial part of the force–displacement curve exhibits an inflection point due to the settling of the specimen and its indentation by the punch, as shown in Fig. 2. Then, the maximum slope corresponding to the slope at the inflection point has to be chosen for the tangent. Regarding the two-tangent method, two tangent lines are drawn for the elastic and plastic bending regions of the force–displacement curve and the force value at the intersection of these two lines is regarded as F_e [1,6,22].

Another method is described in the CEN Workshop Agreement on the Small Punch Test Method for Metallic Materials, CWA 15627:2007, henceforth referred to as the Code-of-Practice (CoP) for SP testing [23]. The two-secant method uses a bilinear regression fit in that F_e derives from the intersection of linear regression lines to the force–displacement curve which are chosen to minimize the error between these straight lines and the SP curve. F_e is

then chosen as the vertical projection of the intersection point to the force–displacement curve.

Table 1 provides a compilation of experimental values for α as proposed in various references. A huge variability of α and a concomitant uncertainty of σ_y are noted which impedes the application of SP tests for a reliable determination of the yield stress. This uncertainty does not only originate from different procedures which have been used for the determination of the elastic–plastic transition force F_e. It also stems from the impossibility of relating the yield stress σ_y to a single force level. In other words, α is an ill-defined parameter: it cannot be considered constant.

In fact, in a recent work, Moreno [17] has systematically investigated the derivation of yield strength from characteristic forces obtained from SP tests of various aluminum alloys and structural steels thereby varying the disc thickness and applying different methodologies for the determination of the elastic–plastic transition force F_e figuring in Eq. (1). The study confirms a huge variability of the coefficients in the range $0.23 \leq \alpha \leq 0.98$ as determined by the various methods applied to the different materials. For the offset method alone, using $h/10$ as the offset, α varied between 0.23 and 0.49. It is concluded that a strong material dependence of the correlation factor α prevents a reliable prediction of the yield stress from F_e. Instead the author suggests using plastic energy as a criterion for establishing σ_y.

Priel et al. [24] carried out finite element (FE) simulations to determine the transition force F_e and used Eq. (1) to extract the coefficient α for different materials and disc thicknesses. Their results revealed a dependence of α on the thickness, which they fitted to an exponential expression giving $\alpha = 0.290$ for the standard thickness $h = 0.5$ mm.

Janča et al. [16] developed a new criterion to assign a correlation force as $F_{e1.5}$ which is based on the equivalence of areas, namely the point of the force–displacement curve, for which the area under the curve (i.e., the energy) is 1.5 times bigger than the complementary area above the curve. The authors report a closer correlation with σ_y as compared to the CoP method when $F_{e1.5}$ is used according to

$$\sigma_y = \alpha \frac{F_{e1.5}}{h^2} + b \,. \qquad (3)$$

Isselin and Shoji [22] have proposed an approach based on elastic energy instead of correlating a force value on the force–displacement curve with yield strength. They considered the elastic energy E_{el} which relates to the square of the stress as:

$$E_{el} = \sigma_y^2 \frac{2[1-\nu^2]R^2h}{3E\pi[1+\nu]^2} \,, \qquad (4)$$

where E is the elastic modulus, ν the Poisson ratio, and R the radius of aperture of the lower die. E_{el} was determined experimentally using the load/unload method. The specimens were loaded to a maximum force level where complete plasticization was assured. The specimens were then unloaded at the same rate, the elastic reverse displacement measured, and the area under the force–displacement curve up to elastic reverse displacement calculated as E_{el}. Hence, instead of identifying an elastic–plastic transition force, a load/unload test is required for this energy-based method, so as to evaluate the area under the elastic part of the force–displacement relation.

In yet another method proposed recently, Calaf Chica et al. [25] combine a finite element analysis with experimental SP tests of different steels to correlate the yield stress with the SP data. They propose an exponential expression for the yield stress σ_y as a function of the slope at the first inflection point, as mentioned before in conjunction with the offset method. In practice, however, one has to note that this slope is strongly affected by the accuracy with
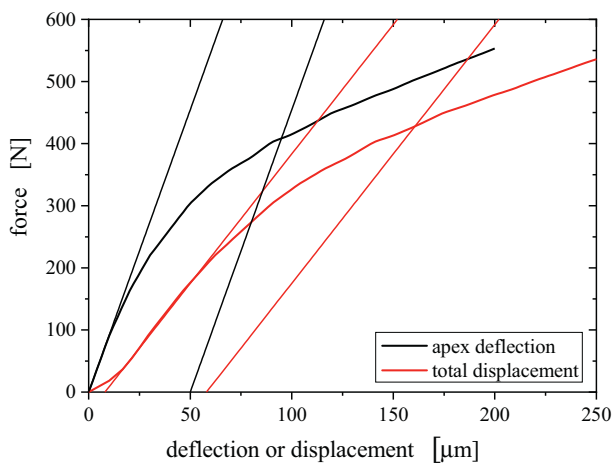

Fig. 2. Illustration of the effect of initial plastic indentation and/or settling of the specimen in its fixture (leading to a positive curvature at the origin and the appearance of an inflection point), as well as the effect of frame compliance (leading to reduced slope at the inflection point). Correspondingly, the elastic–plastic transition force F_e is underestimated, while $\alpha = h^2\sigma_y/F_e$ is overestimated.

which the frame compliance is corrected so that the exponential dependence of σ_y will introduce significant uncertainties.

In this study, a new procedure to establish a robust correlation between σ_y and F_e is developed for ductile metallic materials. To this end, consideration is given to a proper definition of F_e based on FE simulations with discs of different thicknesses in the range of 0.2 to 1 mm. While an offset of 50 μm is confirmed to be a proper choice for the standard disc thickness of 0.5 mm, it is shown that a $\sigma_y - F_e$ correlation cannot be established by a single force level. This is why the curvature of the force–displacement curve will rather be taken into account in a proposal for a new $\sigma_y - F_e$ relation.

2. Numerical modelling of the Small Punch test

A 2D axisymmetric model of the SP test was configured in the finite element program ABAQUS/Standard, see Fig. 3. The dies and the punch are modelled as rigid bodies and the disc as a deformable body. The interaction between the rigid and deformable bodies is implemented by a friction coefficient μ = 0.25 for the punch–disc interface and μ = 1 for the die–disc interface, in order to mimic the clamping effect and foreclose relative tangential motion. The punch was assigned a constant velocity of 0.005 mm/s for which quasi-static conditions prevail [26,27].

Uniform meshing was used with 0.005 mm × 0.005 mm CAX4R elements (axisymmetric continuum stress and displacement, 4-node, reduced-integration element). For the investigated SP disc thicknesses of $h = 0.2, 0.3, 0.4, 0.5, 0.6, 0.7, 0.8$, and 1.0 mm, this corresponds to 40, 60, 80, 100, 120, 140, 160 and 200 through thickness elements, respectively.

Unlike Refs.[26,27], where a Gurson-type porous plasticity model was formulated, the current work uses an isotropic hardening J_2 plasticity model. This proves fully sufficient for the present investigation of the initial yield stage of the material while the absence of damage results in overestimating local strains only at the later stages of SP disc deformation, see, e.g., Fig. 4 (a). Moreover, a direction independent linear elastic stress definition is used with the assumption of small elastic strains, which is justified for metal elasto-plasticity.
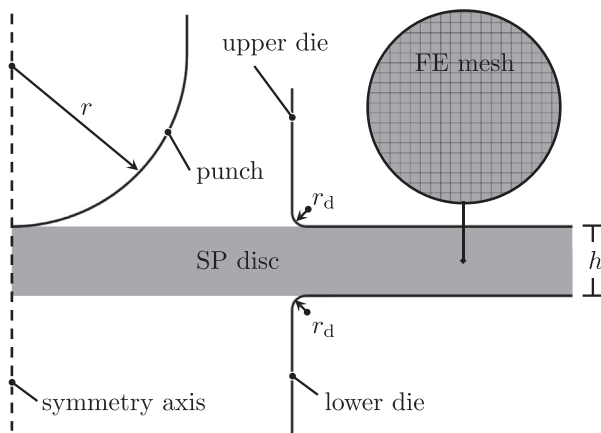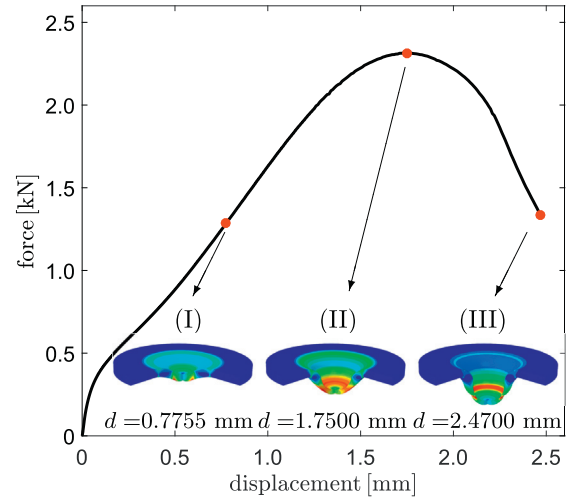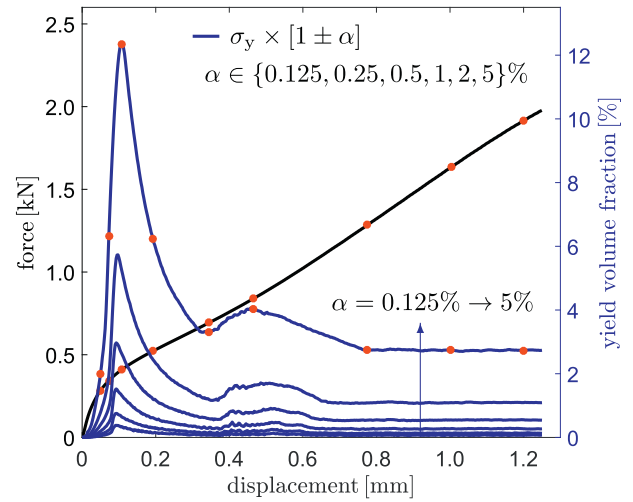

(a)

(b)

Fig. 4. Simulation results for (a) the force–displacement curve together with illustrations of the deformation states at three different displacement levels (in mm), and (b) initial part of the force (left scale) and yield volume fractions (right scale) as functions of displacement and as calculated for six different yield intervals from 0.125% to 5% of the yield stress. In (b), the points marked correspond to deformation stages given in Fig. 5 (a) to (i). Punch displacement is denoted by *d*.

Fig. 3. Idealized axisymmetric FE model for an SP disc of thickness $h = 0.5$ mm, see Fig. 1. The SP disc domain is meshed uniformly with 0.005 mm × 0.005 mm CAX4R elements yielding 100 elements through thickness. Besides accuracy of the solution itself, this also provides accuracy in the integrations regarding the yield volume fraction given in Fig. 4 (b). The punch and die geometries are kept constant with $r = 1.25$ mm and $r_d = 0.1$ mm for all the investigated SP disc thicknesses of $h = 0.2, 0.3, 0.4, 0.5, 0.6, 0.7, 0.8$, and 1.0 mm.

During metal forming processes strain hardening is prevalent. This can be described by power law or exponential hardening rules such as the following
Ludwik rule [28]:

$$\sigma = \sigma_0 + C\epsilon^n, \tag{5}$$

Hollomon rule [29]:

$$\sigma = C\epsilon^n, \tag{6}$$

Swift rule [30]:

$$\sigma = C[\epsilon_0 + \epsilon]^n, \tag{7}$$

Voce rule [31]:

$$\sigma = \sigma_0 + \sigma_\infty[1 - \exp(-\epsilon/\epsilon_0)] \,, \tag{8}$$

the parameters of which are usually determined from uniaxial tensile tests. Satisfactory agreement between these hardening forms and a wide range of experimental material data has been obtained. In the numerical simulations of this work, the two-parameter Hollomon and the three-parameter Ludwik hardening functions are used. To this end, plastically isotropic hardening functions are implemented with the UHARD subroutine interface of ABAQUS. The used strength coefficients C, hardening exponents n, and elastic modulus parameters are reported on the subsequent pages.

3. The elastic–plastic transition force in Small Punch tests

In order to establish a relation for the yield stress σ_y, one first has to establish a transition force F_e from a force–displacement curve. In this study, SP discs of different thicknesses were used in finite element simulations to identify F_e as a function of thickness.

An FE model of the SP test utilizing the constitutive stress–strain curve from a uniaxial tensile test of P91 steel with σ_y identified as the 0.2% offset strain was configured in ABAQUS. For the disc thickness $h = 0.5$ mm, the deformation history was screened to single out the state for which the volume fraction of equivalent stresses close to the yield stress is maximum. To this end, a yield stress interval was defined as $(1 \pm 1\%)\sigma_y$, so as to determine for each time step the zone of the specimen which has equivalent stresses within the σ_y interval defined. F_e was then identified as the force at which the fraction of elements affected by yielding exhibited a maximum with respect to time (see Fig. 4 (b)).

For this purpose, a script was implemented to automise the procedure of finding the volume fraction. This is realised by the implemented USDFLD subroutine. For each time step the (reduced integration) elements with Gauss points whose von Mises stresses are within the interval $\sigma_y(1 - \alpha, 1 + \alpha)$ with $\alpha \in \{0.125, 0.25, 0.5, 1, 2, 5\}\%$ were determined. Since the model is axisymmetric and all elements have equal areas, the fraction of the volume in the yield stress interval, which is hereby referred to as the

yield volume fraction, was then computed as

$$\text{yield volume fraction} = \frac{\sum_{I \in \mathcal{I}_{GP,yld}}^{N_{GP}} r_I}{\sum_J^{N_{GP}} r_J} \,. \tag{9}$$

Here, N_{GP} is the total number of Gauss points (or reduced integration elements) and $\mathcal{I}_{GP,yld}$ the set of Gauss points whose von Mises stress values fall in the yield stress interval $\sigma_y(1 - \alpha, 1 + \alpha)$. r_I denotes the radius at which the Gauss points are positioned.

Fig. 4 depicts simulation results for (a) just the force–displacement curve and (b) the force–displacement curve combined with the yield volume fractions computed for different yield intervals $\sigma_y(1 - \alpha, 1 + \alpha)$ using a three-parameter Ludwik-type hardening rule (Eq. (5)) for P91 steel, the parameters of which are identified from uniaxial tensile test data with curve fitting giving $\sigma_0 = 394$ MPa, $C = 769$ MPa and $n = 0.312$. Here, $\sigma_y = 504.7$ MPa corresponds to the yield stress at 0.2% offset strain. Locally computed maximum equivalent plastic strains are 0.485 for (I), 0.937 for (II) and 2.76 for (III). Severe necking is observed at deformation stage (III). Since no damage is implemented, the local strain values reached are overestimated.

Ternary deformation maps of the nine selected displacement levels of Fig. 4 (b) are shown in Fig. 5. Hereby, the black zones indicate von Mises stress levels at yield within $\pm 5\%$ of the yield stress, while the orange and blue zones exhibit stresses below and above the yield band, respectively. The stress map Fig. 5 (c) featuring a displacement $u = 0.1075$ mm corresponds to the maximum of the yield volume fraction as depicted in Fig. 4 (b). The alternation of colour patterns which is most pronounced in strain map (c) is due to the fact that one actually has different yield zones on the top surface: compressive around the punch contact area and tensile between the punch and the clamped part. Both zones expand as the displacement progresses. As the tensile stretched region hardens, it decomposes into two black rings with a blue ring in between.

The maxima of the yield volume fractions in Fig. 4 (b), while their position weakly depends on the yield interval chosen, are sufficiently pronounced to provide a clear means to identify an elastic–plastic transition force F_e as a function of the punch displacement d. The value of F_e can then be used for the identification of a proper offset as

(a) $d = 0.0500$ mm   (b) $d = 0.0725$ mm   (c) $d = 0.1075$ mm

(d) $d = 0.1925$ mm   (e) $d = 0.3450$ mm   (f) $d = 0.4655$ mm

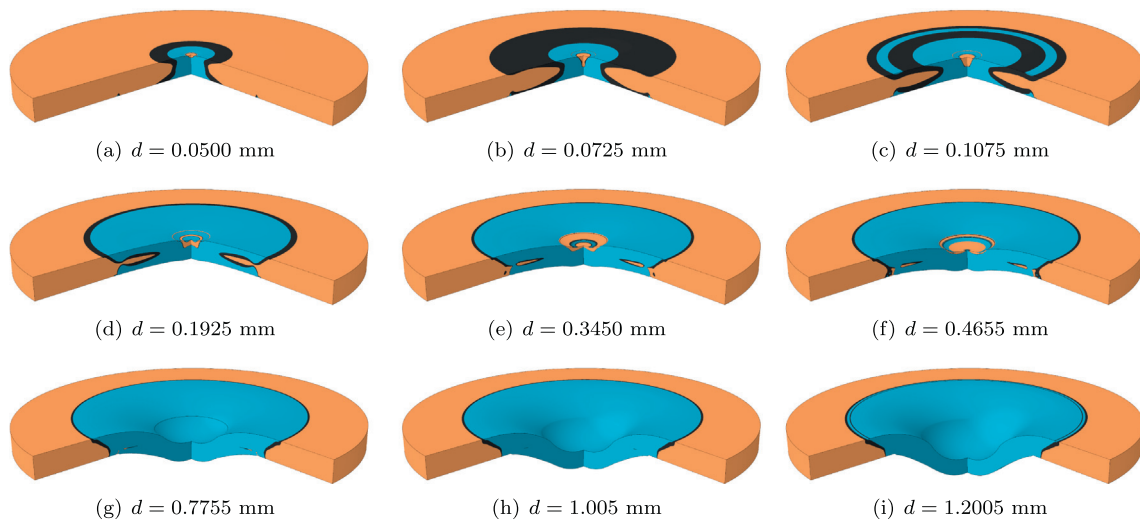(g) $d = 0.7755$ mm   (h) $d = 1.005$ mm   (i) $d = 1.2005$ mm

Fig. 5. Ternary stress maps for different loading stages. The indication of the colour-coding is as follows: Blue represents $\sigma_{vM} > 1.05\sigma_y$, black represents $0.95\sigma_y < \sigma_{vM} < 1.05\sigma_y$ and orange represents $\sigma_{vM} < 0.95\sigma_y$. Punch displacement is denoted by d. (For interpretation of the references to color in this figure legend, the reader is referred to the web version of this article.)
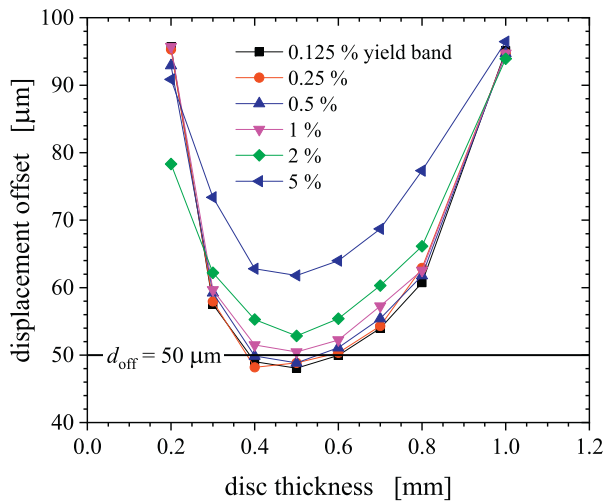
(a)
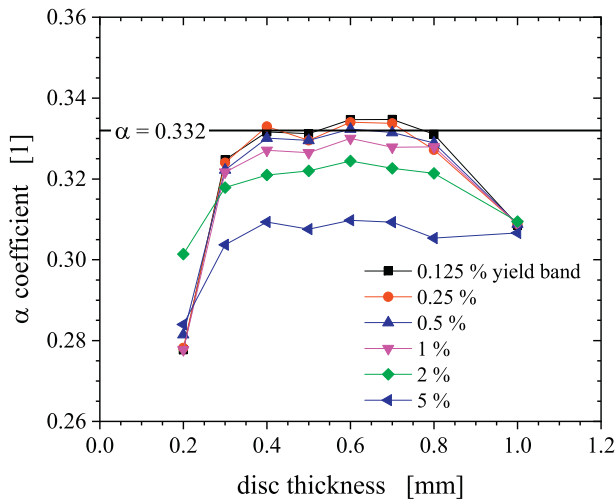
(b)

Fig. 6. Displacement offset d_{off} corresponding to the elastic–plastic transition force F_e (a) and resulting correlation coefficient α (b) as functions of the disc thickness, and calculated for various yield band widths from 0.125% to 5%. As the yield band width decreases, one observes convergence towards $d_{off} \approx 50\mu m$ and $\alpha = 0.332$, respectively.

illustrated by Fig. 6. Using again the material parameters from uniaxial tensile tests of P91, the thickness dependence of the transition force $F_e(h)$ as determined by the maxima of the yield volume fractions in Fig. 4 (b) has been simulated. The disc thicknesses amounted to 0.2; 0.3; 0.4; 0.5; 0.6; 0.7; 0.8; and 1.0 mm. In each case, and for the different yield band width indicated in Figs. 4 (b) and 6(a), the offset was determined that is needed to recover $F_e(h)$ as the intersection point if a tangent is applied to the initial inflection point of the force–displacement curve. In this way, the elastic behaviour was associated with the steepest part of the $F(u)$ curve, as discussed before in conjunction with Fig. 2.

Fig. 6 (a) demonstrates that the displacement offsets which have to be chosen exhibit minima converging at about $d_{off} \approx 50\mu m$ for the narrowest yield band of 0.125% the position of which are close to the thickness of interest, i.e. $h = 0.5$ mm. On the one hand, this confirms $d_{off} = 50\mu m$ as a good choice for the determination of the transition force of 0.5 mm discs. On the other hand, the existence of the minima

is at variance with the notion $d_{off} = h/10$ if the thickness deviates from the standard value, while the radii of the punch and the die aperture are not scaled accordingly.

From the knowledge of the transition forces and the yield stress, one can infer the coefficients α according to Eq. (1) for this specific steel P91. The results are depicted in Fig. 6 (b), suggesting $\alpha = 0.332$ as appropriate for P91, if one averages the values numerically obtained for the three thicknesses 0.4; 0.5; and 0.6 mm and the three narrowest yield band widths investigated: 0.125; 0.25; and 0.5%. As a comparison with the experimental findings compiled in Table 1 reveals, this α value can be considered a lower bound to the reported experimental values, if the value from Matocha et al. [7] which was obtained using twice as big an offset of 100 μm is not taken into account. It has to be kept in mind, however, that the present α value has been established for a single material only, while there is evidence that α is strongly material dependent. This will be investigated in the following sections.

4. Derivation of a new scheme for the yield stress

With a clear definition of the elastic–plastic transition force F_e and the corresponding offset, one can identify a correlation coefficient $\alpha = h_0^2 \sigma_y / F_e$ for a specific material. In general, however, α is not expected to be a constant which is independent of the actual elastic and plastic properties of the material. In fact, Fig. 5 shows that the elastic–plastic transition force F_e relates to a complex yield pattern which involves bending and stretching of the material. Therefore it is not possible to identify a unique value for any kind of material, the main reason being the neglect of the actual strain hardening behaviour of the material. In what follows, a generalized approximation for the yield stress σ_y with improved predictive capability is developed that is still sufficiently simple to serve for rapid material property screening for engineering applications.

If one is to take into account the hardening behaviour, it is not sufficient to work with a single force at a certain offset, e.g. the force at 50 μm offset which is denoted as F_{50}. Instead a triplet of forces at different offsets is to be considered so as to capture the curvature of the force–displacement curve.

As illustrated by Fig. 7, offsets of 10 μm, 50 μm and 90 μm are chosen, defining force triplets $\{F_{10}, F_{50}, F_{90}\}$. The curvature of the
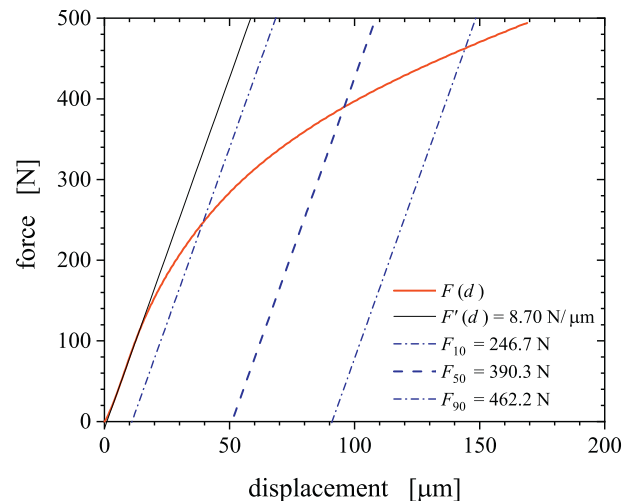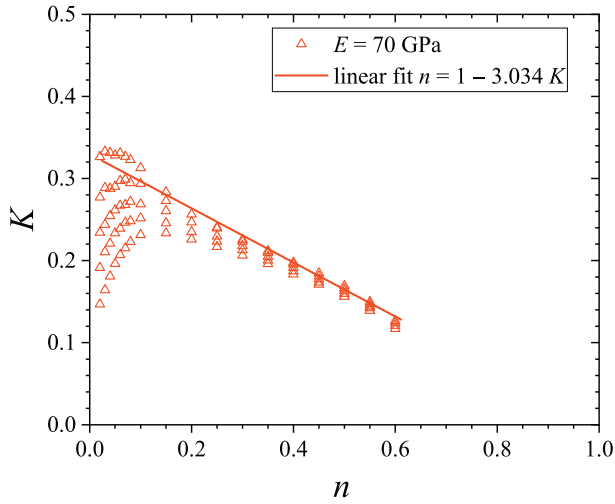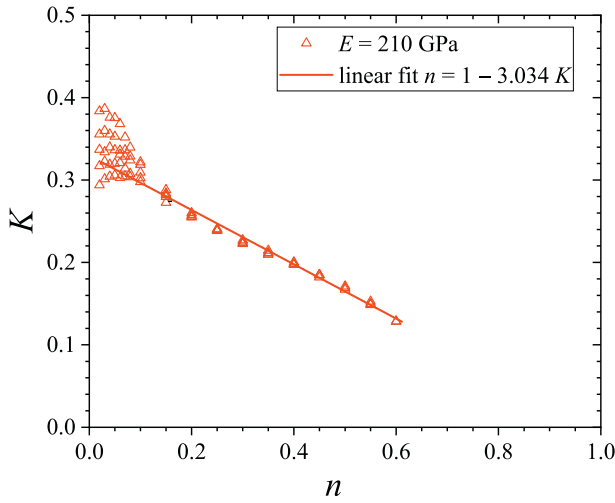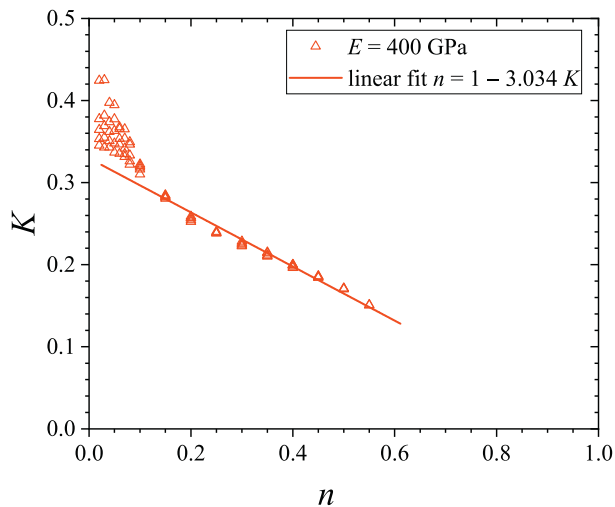

Fig. 7. Illustration of a scheme to quantify the curvature of the force–displacement curve by identifying the levels at three distinct displacement offsets, i.e. 10 μm, 50 μm and 90 μm. The data indicated pertain to the FE simulation of P91 steel as introduced in Section 3.

(a)

(b)

(c)

Fig. 8. Dependence of the curvature factor K on the hardening exponent n as numerically determined for a variety of Hollomon-type power law hardening rules with strength coefficients $300\,\text{MPa} < C < 1500\,\text{MPa}$ and $0.02 < n < 0.6$ for (a) $E = 70\,\text{GPa}$, (b) $E = 210\,\text{GPa}$, (c) $E = 400\,\text{GPa}$.

force–displacement curves is numerically determined for a variety of Hollomon-type hardening rules, $\sigma = C\epsilon^n$, for wide ranges of strength coefficients $(300\,\text{MPa} < C < 1500\,\text{MPa})$ and hardening exponents $(0.02 < n < 0.6)$ while three different values for the elastic modulus are used: $E = 70\,\text{GPa}$, $E = 210\,\text{GPa}$ and $E = 400\,\text{GPa}$. The Poisson ratio is chosen as $\nu = 0.3$. The curvature of the force–displacement curve is then quantified by a dimensionless curvature factor K defined as

$$K = 2\frac{F_{50} - F_{10}}{F_{90} - F_{10}} - 1 = \frac{[F_{50} - F_{10}] - [F_{90} - F_{50}]}{F_{90} - F_{10}} \ . \tag{10}$$

From simulations of the two-parameter hardening rule (Eq. (6)), one gets a relationship between the curvature K and the hardening exponent n, which can be approximated by a straight line. From a linear fit for $0.1 \leq n \leq 0.6$ for $E = 210\,\text{GPa}$, one obtains:

$$n = 1 - 3.034K \quad \text{for} \quad K < 0.330 \ . \tag{11}$$

This is shown in Fig. 8 (b), while Fig. 8 (a) and (c) illustrates the quality of the same fit line as applied to simulation results for $E = 70\,\text{GPa}$ and $E = 400\,\text{GPa}$, respectively. The fit works well for the intermediate level $E = 210\,\text{GPa}$. However, K is overestimated at small n values for $E = 70\,\text{GPa}$, whereas it is underestimated for $E = 400\,\text{GPa}$. These deviations are brought about by a dependence of K on the strength coefficient C, which is insignificant for the larger values of n.

It is important to note that the hardening exponent n can be inferred from the curvature K in a way as to derive a K-dependent yield coefficient α_{50} and the corresponding yield stress σ_y. A linear fit to the $E = 210\,\text{GPa}$ data gives

$$\alpha_{50} = 0.360 - 0.422n \quad \text{for} \quad n > 0 \ . \tag{12}$$

Regarding Fig. 9 (a–c), the quality of the fit is very satisfactory, in particular, for the two higher values of Young's moduli (Fig. 8 (a–c)).

If one combines Eqs. (11) and (12), the n-dependence of α_{50} translates into a stepwise linear K-dependence

$$\alpha_{50} = \begin{cases} 1.28K - 0.062 & \text{for} \quad K < 0.330 \ , \\ 0.360 & \text{otherwise} \ , \end{cases} \tag{13}$$

where the step at $K = 0.330$ is required by the necessity to consider positive n values only. This is illustrated in Fig. 10 showing that the accuracy of the stepwise linear approximation increases with increasing E. The K-dependence of α_{50} leads to the following K-dependent yield stress as derived from the force at $50\,\mu\text{m}$ offset:

$$\sigma_y = \begin{cases} [1.28K - 0.062]\frac{F_{50}}{h^2} & \text{for} \quad K < 0.330 \ , \\ 0.360\frac{F_{50}}{h^2} & \text{otherwise} \ . \end{cases} \tag{14}$$

In practice, this can be used to derive the yield stress based on the knowledge of three forces determined at three different offsets of $10\,\mu\text{m}$, $50\,\mu\text{m}$ and $90\,\mu\text{m}$, which gives more reliable results for a wide range of hardening behaviours as compared to the traditional method based on F_{50} determined at $50\,\mu\text{m}$ offset only. In the following section, the present 10-50-90 offset scheme is validated by comparing it to the predictive performance of the traditional scheme for which $\alpha_{50} = 0.360 = \text{constant}$ is used for the ease of comparability.
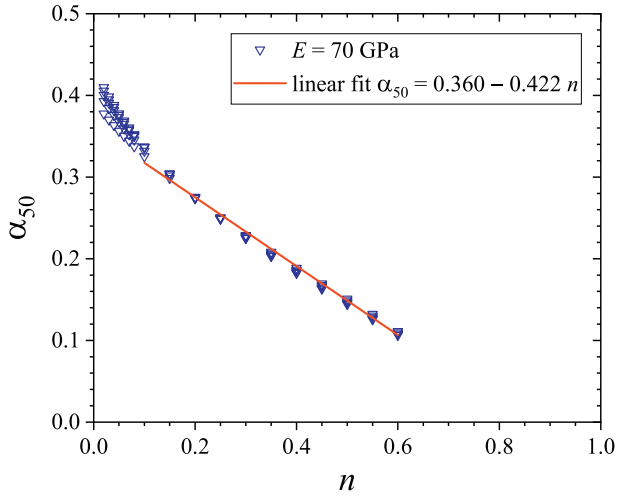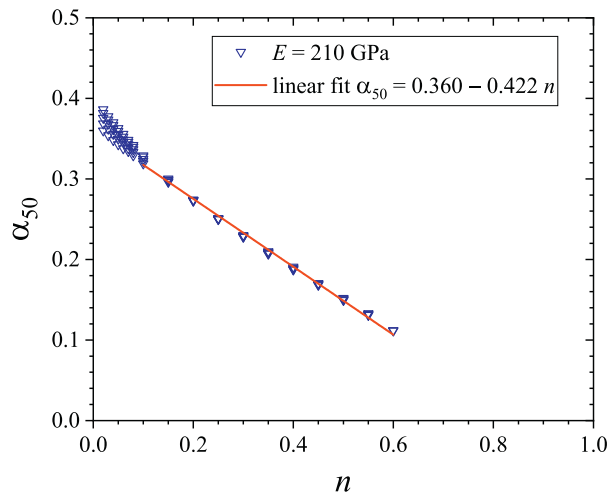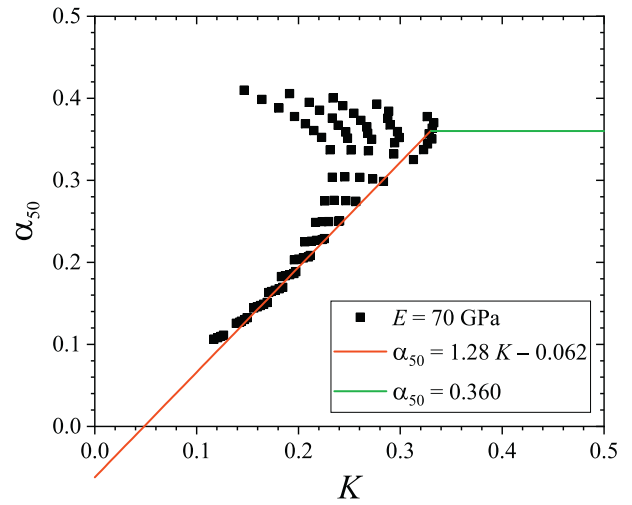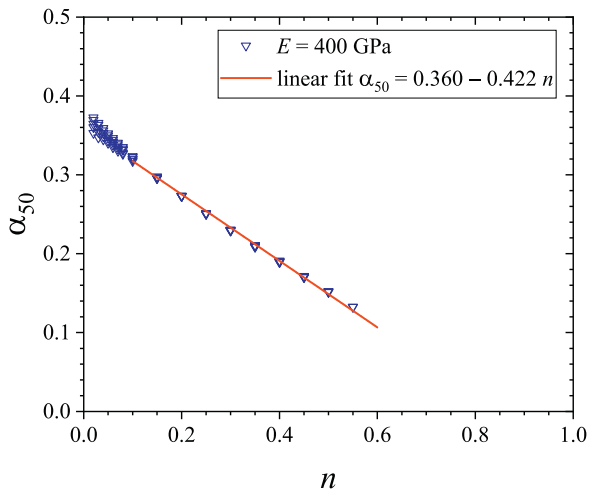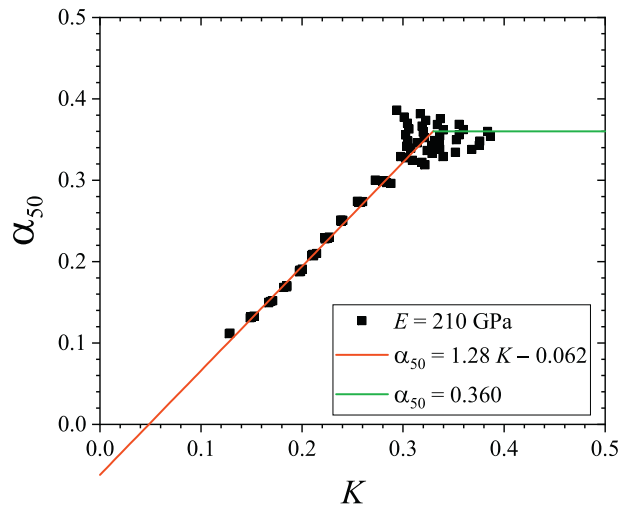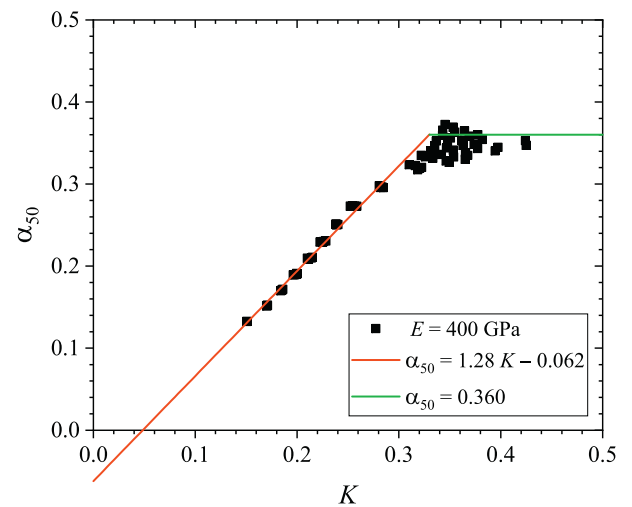
Fig. 9. Correlation factor $\alpha_{50} = h_0^2 \sigma_{y,nom}/F_{50}$ as a function of hardening exponent n numerically determined for power law hardening rules with strength coefficients $300\,\text{MPa} < C < 1500\,\text{MPa}$ and $0.02 < n < 0.6$ for (a) $E = 70\,\text{GPa}$, (b) $E = 210\,\text{GPa}$, (c) $E = 400\,\text{GPa}$.

Fig. 10. The curvature dependence of the correlation factor $\alpha_{50} = h_0^2 \sigma_{y,nom}/F_{50}$ for power law hardening rules with strength coefficients $300\,\text{MPa} < C < 1500\,\text{MPa}$ and $0.02 < n < 0.6$ for (a) $E = 70\,\text{GPa}$, (b) $E = 210\,\text{GPa}$, (c) $E = 400\,\text{GPa}$.

(a)

(b)

(c)

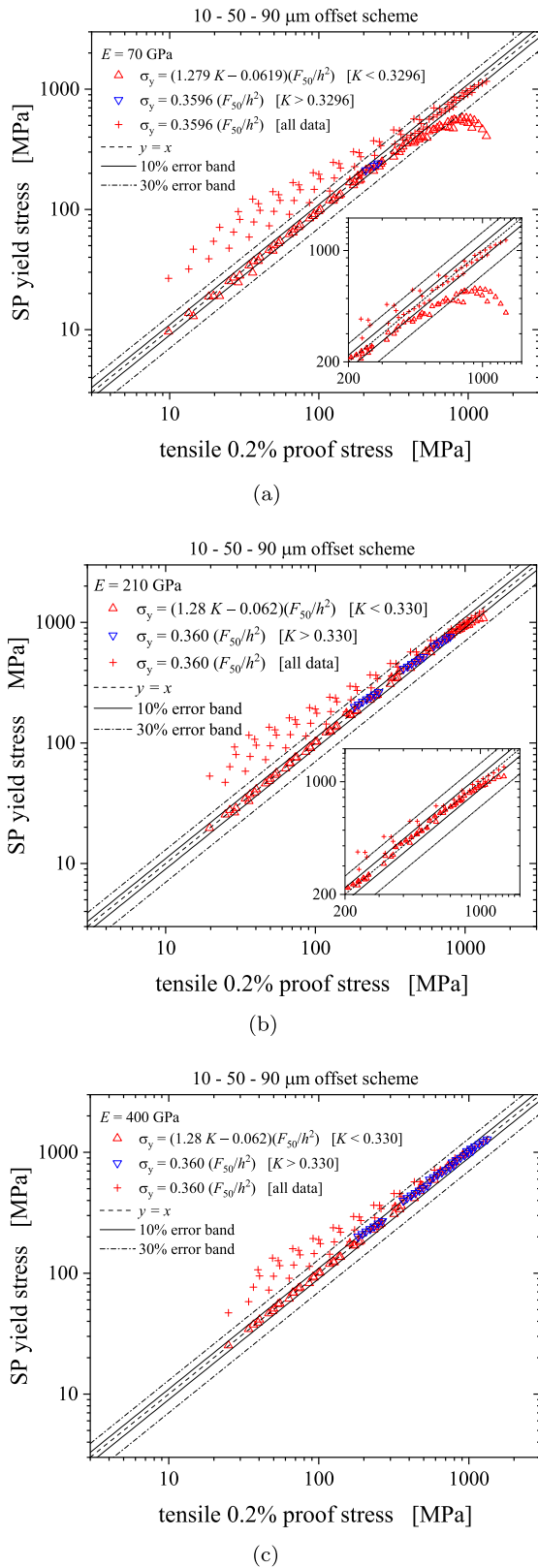**Fig. 11.** Predicted SP yield stress vs. input 0.2% proof stress for power law harden-ing rules with strength coefficients 300 MPa $< C <$ 1500 MPa and 0.02 $< n <$ 0.6 for (a) $E = $ 70 GPa, (b) $E = $ 210 GPa, (c) $E = $ 400 GPa; comparison of the present curvature-based offset scheme (red and blue triangles for $K <$ 0.330 and $K >$ 0.330, respectively) with the usual offset scheme (red crosses) using $\alpha_{50} = $ 0.36 for all K values, not limited to $K >$ 0.330 as proposed in the present work. (For interpretation of the references to color in this figure legend, the reader is referred to the web version of this article.)

5. Validation of the scheme

The predictive capability of the proposed 10-50-90 µm offset scheme is determined by comparing the SP based yield stresses as derived from the three different displacement offsets with the actual tensile 0.2% proof stresses implemented in the FE simulations. The validation is hence based on numerical rather than experimental data which would be affected by additional uncertainties and sys-tematic errors associated with the equipment and testing protocols used. The traditional scheme with $\alpha_{50} = $ 0.360 $=$ constant serves as a benchmark.

In Fig. 11, the SP yield stress as predicted by the present 10-50-90 µ m offset scheme is compared with the actual 0.2% proof stress corresponding to the power law hardening rules with strength coefficients and hardening exponents again covering the ranges 300 MPa $< C <$ 1500 MPa and 0.02 $< n <$ 0.6, respectively, for (a) $E = $ 70 GPa, (b) $E = $ 210 GPa, (c) $E = $ 400 GPa. The superior performance of the present curvature-based offset scheme (red and blue triangles for $K <$ 0.330 and $K >$ 0.330, respec-tively) as compared to the usual offset scheme (red crosses) using $\alpha_{50} = $ 0.36 for all K values, hence not limited to $K >$ 0.330, is clearly visible. The degree of agreement increases with increasing Young's modulus. While the traditional correlation $\alpha = h_0^2 \sigma_y / F_e = $ constant may lead to overestimating the yield stress by more than 100%, the present scheme significantly improves the property correlation accuracy.

Fig. 12 shows the performance of the present scheme in terms of the error percentage of the predicted SP yield stress vs. normalized input 0.2% proof stress $\sigma_{y,nom}/E$ for power law hardening rules with strength coefficients 300 MPa $< C <$ 1500 MPa and 0.02 $< n <$ 0.6 for $E = $ 70 GPa (blue squares), as well as the worst performing three data points selected for $E = $ 210 GPa (red triangles). Three parameter domains are identified with poor predictive power, that is domains where the relative error exceeds 10%: (i) for soft materials with strong hardening capacity ($n = $ 0.6) and low elastic modu-lus ($E = $ 70 GPa), (ii) for high strength materials with $\sigma_{y,nom}/E >$ 3 $\times$ 10^{-3} and $E = $ 70 GPa and (iii) for $\sigma_{y,nom}/E >$ 1.6 $\times$ 10^{-2}
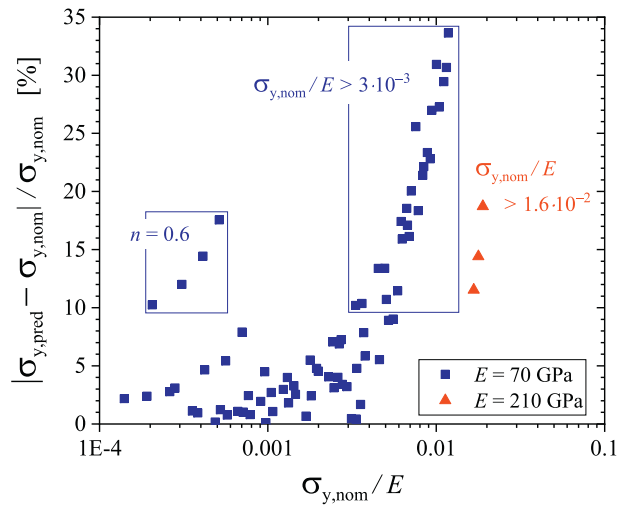

Fig. 12. Error percentage of the predicted SP yield stress vs. normalized input 0.2% proof stress $\sigma_{y,nom}/E$ for power law hardening rules with strength coefficients 300 MPa $< C <$ 1500 MPa and 0.02 $< n <$ 0.6 for $E = $ 70 GPa (blue squares) and worst performing data selected for $E = $ 210 GPa (red triangles). (For interpretation of the references to color in this figure legend, the reader is referred to the web version of this article.)

Table 2
Scheme validation through numerical results obtained from simulating the F/M steel P91, the RPV steel A533B, and the Ni-base superalloy U720pm. The latter two materials exhibit yield phenomena. For comparison results of power law flow with similar yield stresses, however, without yield phenomena are also compiled.

	10-50-90 scheme				
	P91 (numerical)	A533B (numerical)	$C = 900\,\mathrm{MPa}$ $n = 0.1$	U720pm (numerical)	$C = 1500\,\mathrm{MPa}$ $n = 0.05$
10 µm offset force F_{10} [N]	247	229	235	459	465
50 µm offset force F_{50} [N]	390	375	372	779	757
90 µm offset force F_{90} [N]	462	437	445	930	913
Curvature factor K	0.333	0.402	0.309	0.357	0.306
α_{50} factor	0.360	0.360	0.333	0.360	0.330
0.2% proof stress [MPa]	505	500	483	1100	1099
Predicted yield stress [MPa]	561	539	497	1120	998
Relative error [%]	11	8	3	2	3

and $E = 210\,\mathrm{GPa}$. So one concludes that the predictive power of the 10-50-90 µm offset scheme decreases with increasing strength and strain hardening rate, if it goes along with low elastic modulus. However, $\sigma_{y,nom}/E > 1.6 \times 10^{-2}$ is outside the scope of real metallic materials apart from the strongest titanium alloys like Ti6Al4V which may reach up to $\sigma_{y,nom} = 1200\,\mathrm{MPa}$, and $\sigma_{y,nom}/E$ values of up to 10^{-2}, while $E = 120\,\mathrm{GPa}$ is in between the values of 70 GPa and 210 GPa considered here.

Furthermore, the 10-50-90 µm offset scheme is used to predict the yield stresses of three other materials, without making use of the two-parameter hardening rule of the Hollomon type. Table 2 shows numerical results obtained from simulating the F/M steel P91, the reactor pressure vessel (RPV) steel A533B, and the Ni-base superalloy U720pm. For P91 the three-parameter Ludwik-type hardening rule $\sigma = \sigma_0 + C\epsilon^n$ with $\sigma_0 = 394\,\mathrm{MPa}$, $C = 769$, $n = 0.312\,\mathrm{MPa}$ was used, which gives rise to a tensile yield stress $\sigma_y = R_{p0.2} = 505\,\mathrm{MPa}$, see Fig. 7 regarding the forces indicated. For A533B and U720pm, which both exhibit yield phenomena, the experimental tensile stress–strain data were implemented with tensile yield stresses $\sigma_y = R_{p0.2} = 500\,\mathrm{MPa}$ and 1100 MPa, respectively, as shown in Figs. 13 and 14. For comparison results of power law flow with similar yield stresses, however without yield phenomena

are also compiled. The corresponding force–displacement curves, as obtained from the simulations, are compared in Fig. 15.

These industrial materials cover a wide range of applications, while curvatures K approximately vary from 0.3 to 0.4, that is for K values below and above the critical value $K = 0.330$ which marks the transition between the two piecewise linear approximations. The relative errors in predicting the yield stresses vary from 2% to 11%, with the largest error occurring for P91. This is understandable by the fact that for this material the predictive accuracy is reduced, since the curvature $K = 0.333$ happens to be very close to the critical one. The scheme performs well even in the case of materials exhibiting a yield phenomenon.

6. Conclusions

The determination of material degradation of components in service is crucial for the structural integrity and remaining life assessment, especially in power plants. The SP test as a miniaturized test technique enables the screening of the impairment in mechanical properties (elastic, plastic and creep) with minimal material requirements. Yet, the estimation of the yield strength from SP testing suffers from significant uncertainties in the absence of a robust
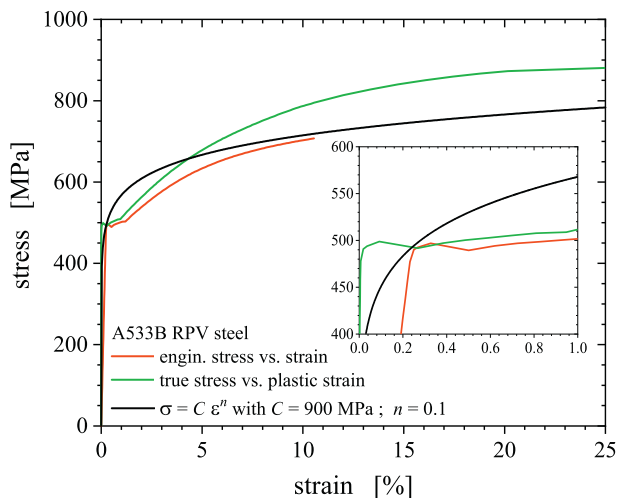

Fig. 13. Tensile engineering (red) and true (green) stress–strain data showing a yield phenomenon for the RPV steel A533B as implemented in the simulation: $\sigma_y = R_{p0.2} = 500\,\mathrm{MPa}$. For comparison a power law hardening rule (black) with similar yield stress is also indicated. (For interpretation of the references to color in this figure legend, the reader is referred to the web version of this article.)

Fig. 14. Tensile engineering (red) and true (green) stress–strain data showing a yield phenomenon for the Ni-base superalloy U720pm as implemented in the simulation: $\sigma_y = R_{p0.2} = 1100\,\mathrm{MPa}$. For comparison a power law hardening rule (black) with similar yield stress is also indicated. (For interpretation of the references to color in this figure legend, the reader is referred to the web version of this article.)
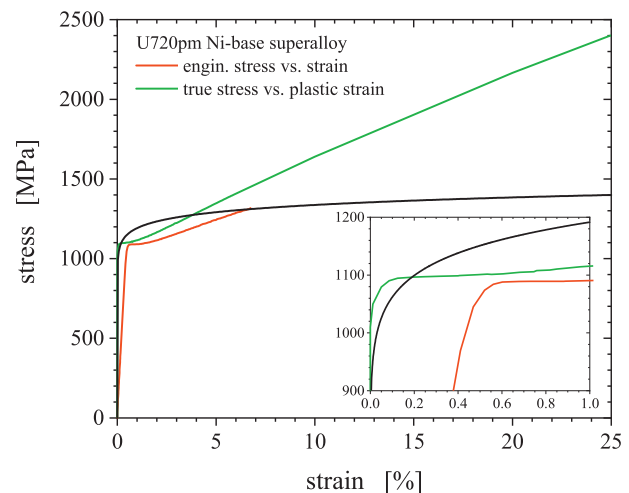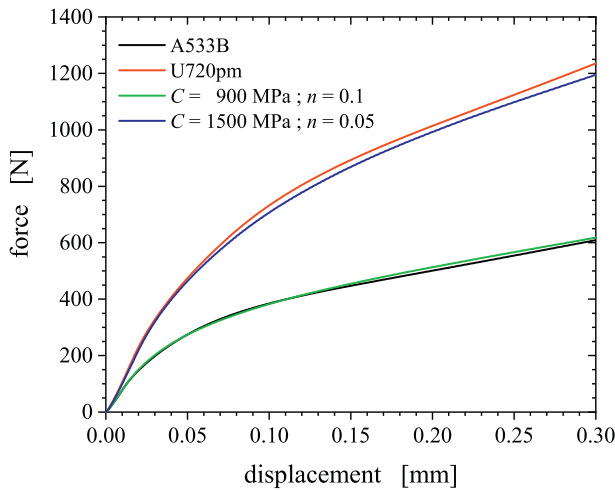
Fig. 15. Simulated SP force–displacement curves for A533B and U720pm, as well as for power law hardening rules exhibiting similar yield stresses $\sigma_y = R_{p0.2} = 500$ and 1100 MPa, respectively, as shown in Figs. 13 and 14 and compared in Table 2.

mechanical property correlation. In this study, a new methodology for estimating the yield stress from SP force–displacement curves was presented that is based on FE simulations of a wide range of constitutive hardening rules.

The tensile yield stress σ_y is commonly associated with an elastic–plastic transition force F_e via $\sigma_y = \alpha F_e / h^2$ with h denoting the SP disc thickness and a dimensionless coefficient α. In the present work it has been shown, however, that α cannot be taken as a constant. The coefficient α rather depends on the strain hardening behaviour of a material (as reflected by the hardening exponent n of power law flow) which, in the absence of knowledge of n, can be inferred from the curvature of the force–displacement curve recorded in the SP test. In practice, this is achieved by determining the forces at three different offsets ($10\,\mu m$, $50\,\mu m$ and $90\,\mu m$ for $h = 0.5$ mm disc thickness), instead of attempting to link the yield stress to a single offset (for which $h/10 = 50\mu m$ has most widely been used).

CRediT authorship contribution statement

Peter Hähner: Conceptualization, Formal analysis, Methodology, Supervision, Validation, Writing - original draft. **Celal Soyarslan:** Data curation, Formal analysis, Investigation, Methodology, Software, Visualization, Writing - review & editing. **Betül Gülçimen Çakan:** Data curation, Investigation, Visualization, Writing - review & editing. **Swantje Bargmann:** Supervision, Writing - review & editing.

References

[1] B. Gülçimen, A. Durmuş, S. Ülkü, R. Hurst, K. Turba, P. Hähner, Mechanical characterisation of a P91 weldment by means of small punch fracture testing, Int. J. Press. Vessel. Pip. 105-106 (2013) 28–35.
[2] T. García, C. Rodríguez, F. Belzunce, C. Suárez, Estimation of the mechanical properties of metallic materials by means of the small punch test, J. Alloys Compd. 582 (2014) 708–717.
[3] J. Kameda, X. Mao, Small-punch and TEM-disc testing techniques and their application to characterization of radiation damage, J. Mater. Sci. 27 (1992) 983–989.
[4] V. Vorlicek, L.F. Exworthy, P.E.J. Flewitt, Evaluation of a miniaturized disc test for establishing the mechanical properties of low-alloy ferritic steels, J. Mater. Sci. 30 (Jan 1995) 2936–2943.
[5] E. Fleury, J. Ha, Small punch tests to estimate the mechanical properties of steels for steam power plant: I. Mechanical strength, Int. J. Press. Vessel. Pip. 75 (9) (1998) 699–706.
[6] X. Mao, H. Takahashi, Development of a further-miniaturized specimen of 3 mm diameter for TEM disk (ϕ3 mm) small punch tests, J. Nucl. Mater. 150 (1) (1987) 42–52.
[7] K. Matocha, M. Filip, S. Stejskalova, Determination of critical temperature of brittleness T_{K0} by small punch tests, Proceedings of COMAT2012 − Recent Trends in Structural Materials, 2012,
[8] M. Bruchhausen, S. Holmström, I. Simonovski, T. Austin, J.-M. Lapetite, S. Ripplinger, F. de Haan, Recent developments in small punch testing: tensile properties and DBTT, Theor. Appl. Fract. Mech. 86 (2016) 2–10. small Scale Testing in Fracture Mechanics.
[9] J. Cheon, I. Kim, Initial deformation during small punch testing, J. Test. Eval. 24 (4) (1996) 255–262.
[10] D. Finarelli, M. Roedig, F. Carsughi, Small punch tests on austenitic and martensitic steels irradiated in a spallation environment with 530 MeV protons, J. Nucl. Mater. 328 (2) (2004) 146–150.
[11] E. Campitelli, P. Spätig, R. Bonadé, W. Hoffelner, M. Victoria, Assessment of the constitutive properties from small ball punch test: experiment and modeling, J. Nucl. Mater. 335 (3) (2004) 366–378.
[12] M.A. Contreras, C. Rodríguez, F.J. Belzunce, C. Betegón, Use of the small punch test to determine the ductile-to-brittle transition temperature of structural steels, Fatigue Fract. Eng. Mater. Struct. 31 (9) (2008) 727–737.
[13] C. Rodríguez, J.G. Cabezas, E. Cárdenas, F.J. Belzunce, C. Betegón, Mechanical properties characterization of heat-affected zone using the small punch test, Weld. Res. 88 (2009) 188–192.
[14] E. Altstadt, H. Ge, V. Kuksenko, M. Serrano, M. Houska, M. Lasan, M. Bruchhausen, J.-M. Lapetite, Y. Dai, Critical evaluation of the small punch test as a screening procedure for mechanical properties, J. Nucl. Mater. 472 (2016) 186–195.
[15] E. Altstadt, M. Houska, I. Simonovski, M. Bruchhausen, S. Holmström, R. Lacalle, On the estimation of ultimate tensile stress from small punch testing, Int. J. Mech. Sci. 136 (2018) 85–93.
[16] A. Janča, J. Siegl, P. Haušild, Small punch test evaluation methods for material characterisation, J. Nucl. Mater. 481 (2016) 201–213.
[17] M. Moreno, Effects of thickness specimen on the evaluation of relationship between tensile properties and small punch testing parameters in metallic materials, Mater. Des. 157 (2018) 512–522.
[18] S. Davies, S. Jeffs, R. Lancaster, G. Baxter, High temperature deformation mechanisms in a DLD nickel superalloy, Materials 10 (2017) 457.
[19] R. Lacalle, J. Álvarez, S. Cicero, F. Gutiérrez-Solana, From archeology to precious metals: four applications of small punch test, Metall. J. 63 (01 2010) 1–10.
[20] Z.-X. Wang, H.-J. Shi, J. Lu, P. Shi, X.-F. Ma, Small punch testing for assessing the fracture properties of the reactor vessel steel with different thicknesses, Nucl. Eng. Des. 238 (12) (2008) 3186–3193.
[21] Y.W. Ma, K.B. Yoon, Assessment of tensile strength using small punch test for transversely isotropic aluminum 2024 alloy produced by equal channel angular pressing, Mater. Sci. Eng. A 527 (16) (2010) 3630–3638.
[22] J. Isselin, T. Shoji, Yield strength evaluation by small-punch test, J. Test. Eval. 37 (11 2009) 531–537.
[23] CWA 15627:2007, Small Punch Test Method For Metallic Materials, CEN Workshop Agreement, 2007,
[24] E. Priel, B. Mittelman, S. Haroush, A. Turgeman, R. Shneck, Y. Gelbstein, Estimation of yield and ultimate stress using the small punch test method applied to non-standard specimens: a computational study validated by experiments, Int. J. Mech. Sci. 135 (2018) 484–498.
[25] J. Calaf Chica, P.M. Bravo Díez, M. Preciado Calzada, Development of an improved prediction method for the yield strength of steel alloys in the Small Punch Test, Mater. Des. 148 (2018) 153–166.
[26] C. Soyarslan, B. Gülçimen, S. Bargmann, P. Hähner, Modeling of fracture in small punch tests for small- and large-scale yielding conditions at various temperatures, Int. J. Mech. Sci. 106 (2016) 266–285.
[27] B. Gülçimen Çakan, C. Soyarslan, S. Bargmann, P. Hähner, Experimental and computational study of ductile fracture in small punch tests, Materials 10 (10, article no.=1185). (2017)
[28] P. Ludwik, Elemente der Technologischen Mechanik, Verlag von Julius Springer, Berlin, 1909.
[29] J. Hollomon, Tensile deformation, Trans. AIME 112 (1945) 268–290.
[30] H. Swift, Plastic instability under plane stress, J. Mech. Phys. Solids 1 (1) (1952) 1–18. ISSN 0022-5096.
[31] E. Voce, The relationship between stress and strain for homogeneous deformation, J. Inst. Metals 74 (1948) 537–562.